



**HAL**  
open science

# Wafer-Scale 200 mm Metal Oxide Infrared Metasurface with Tailored Differential Emissivity Response in the Atmospheric Windows

Kai Sun, Evangelos Vassos, Xingzhao Yan, Callum Wheeler, James Churm, Peter Wiecha, Simon A Gregory, Alex Feresidis, Cornelis H de Groot, Otto L. Muskens

## ► To cite this version:

Kai Sun, Evangelos Vassos, Xingzhao Yan, Callum Wheeler, James Churm, et al.. Wafer-Scale 200 mm Metal Oxide Infrared Metasurface with Tailored Differential Emissivity Response in the Atmospheric Windows. *Advanced Optical Materials*, 2022, 10 (17), pp.2200452. 10.1002/adom.202200452 . hal-03822489

**HAL Id: hal-03822489**

**<https://hal.science/hal-03822489>**

Submitted on 20 Oct 2022

**HAL** is a multi-disciplinary open access archive for the deposit and dissemination of scientific research documents, whether they are published or not. The documents may come from teaching and research institutions in France or abroad, or from public or private research centers.

L'archive ouverte pluridisciplinaire **HAL**, est destinée au dépôt et à la diffusion de documents scientifiques de niveau recherche, publiés ou non, émanant des établissements d'enseignement et de recherche français ou étrangers, des laboratoires publics ou privés.

# Wafer-Scale 200 mm Metal Oxide Infrared Metasurface with Tailored Differential Emissivity Response in the Atmospheric Windows

Kai Sun,\* Evangelos Vassos, Xingzhao Yan, Callum Wheeler, James Churm, Peter R. Wiecha, Simon A. Gregory, Alex Feresidis,\* Cornelis H. de Groot, and Otto L. Muskens\*

Metasurfaces with sub-wavelength nanoscale features have emerged as a platform to achieve desirable electromagnetic responses. However, it remains technically challenging to fabricate metasurfaces in large size and at low cost for mass production. This work demonstrates a 200 mm wafer-scale Al:ZnO metasurface coating based on deep-UV lithography. The metasurfaces are targeted to achieve infrared (IR) reflectivity and emissivity characteristics at bandwidths across the two atmospheric windows in the IR spectrum. The wafers demonstrate a high uniformity of optical response with tailored reflectivity of around 50% at the 3–5  $\mu\text{m}$  mid-wave IR band and less than 10% at the 8–13  $\mu\text{m}$  long-wave IR band. This article furthermore shows that the design principle allows achieving a wide range of dual-band reflectivity values using a single underlying materials stack, offering a versatile platform. The proposed approach is compatible with CMOS-compatible mass-production manufacturing and brings IR metasurface coatings closer to commercially relevant and scalable technology.

## 1. Introduction

In the last decade, metasurfaces have shown great potential to tailor optical responses at different wavelength ranges. Using sub-wavelength feature arrays, optical properties can be engineered to strongly enhance light-matter interactions<sup>[1–3]</sup> and achieve electromagnetic control over amplitude,<sup>[4,5]</sup> phase,<sup>[4–6]</sup> and polarization.<sup>[4,5,7]</sup> Significant research has been conducted on metamaterial absorbing surface design at microwave,<sup>[8–14]</sup> terahertz, infrared, and optical frequency bands.<sup>[15–21]</sup> Traditionally, a quarter-wavelength resonator mounted on a resistive sheet is placed at a certain distance from a ground plane to construct an electromagnetic absorber.<sup>[8,21,22]</sup> Numerous periodic metallic structures and substrate materials have been employed to develop metamaterial absorbers for single-band, multi-band, and wideband frequency operations across the mentioned electromagnetic spectrum.

The infrared (IR) spectrum is of particular interest as it covers two transparent windows of the atmosphere, the 3–5  $\mu\text{m}$  mid-wave infrared (MWIR) window and the 8–13  $\mu\text{m}$  long-wave infrared (LWIR) window. Materials with responses tailored to this range have broad applications. In particular, lightweight, low volume, and large-area treatments that are able to control the spectral emissivity profile of surfaces, have been shown to be of interest for thermal management through radiative cooling,<sup>[23–25]</sup> spectrally selective detectors and emitters,<sup>[8,26–32]</sup> infrared imaging,<sup>[28,33,34]</sup> polarization control,<sup>[35–37]</sup> sensing,<sup>[38–42]</sup> and defense.<sup>[43–52]</sup> Engineering of the electromagnetic properties of materials over the different bands in mid-IR is therefore of considerable interest for controlling the reflectivity, absorption, and emissivity spectral response.

Here, we demonstrate a wafer-scale Al:ZnO metasurface fulfilling a dual-band optical response at MWIR and LWIR. Our design approach combines in-plane metasurface and out-of-plane multilayer degrees of freedom, as well as the strong material dispersion of several selected materials, in order to achieve independent control in the two technologically important atmospheric windows with a spectrally flat response within

K. Sun, X. Yan, C. Wheeler, C. H. de Groot, O. L. Muskens  
Faculty of Engineering and Physical Sciences  
University of Southampton  
Southampton SO17 1BJ, UK  
E-mail: k.sun@soton.ac.uk; o.muskens@soton.ac.uk

E. Vassos, J. Churm, A. Feresidis  
Department of Electronic  
Electrical and Systems Engineering  
University of Birmingham  
Birmingham B15 2TT, UK  
E-mail: a.feresidis@bham.ac.uk

P. R. Wiecha  
LAAS  
Université de Toulouse  
CNRS  
Toulouse 31000, France

S. A. Gregory  
Defence Science and Technology Laboratory (Dstl)  
Wiltshire SP4 0JQ, UK

The ORCID identification number(s) for the author(s) of this article can be found under <https://doi.org/10.1002/adom.202200452>.

© 2022 The Authors. Advanced Optical Materials published by Wiley-VCH GmbH. This is an open access article under the terms of the Creative Commons Attribution License, which permits use, distribution and reproduction in any medium, provided the original work is properly cited.

DOI: 10.1002/adom.202200452

the bands. This approach allows covering a large range of parameter space using only a single basic device stack, which enables designer functionality in a single device and materials platform. Our approach is distinct from previous studies involving either multiple narrowband resonators<sup>[32,34,42,53]</sup> or intricate multi-resonator antenna designs<sup>[31,37,41,54]</sup>. We present the experimental realization of this device structure using state-of-the-art cleanroom nanofabrication on 200 mm silicon substrates. In our experimental studies, a homogeneous 200 mm wafer-scale metasurface has been fabricated with a reflectance of around 50% in MWIR and 10% in LWIR. Achieving such uniform functional optical coatings with unique features with optical metasurfaces requires large area fabrication with high fidelity. Fabrication methods capable of producing patterned metasurfaces that cover a large area and in high volume are still lacking. Most reported metasurfaces are fabricated through e-beam lithography (EBL),<sup>[31,34,41,42,55–57]</sup> which is unsuitable for mass production and large area size, or standard photolithography, which is suitable for minimum feature sizes of micrometers.<sup>[46,50,51,54]</sup> Some recent works have adopted deep-ultraviolet (DUV) lithography for metasurface fabrication.<sup>[32,45,58–61]</sup> To achieve large-area device patterning, we make use of a DUV lithography scanner. In this method, a KrF UV laser at 248 nm wavelength is used to project a mask from a reticle onto the fabrication area. The wafer is subsequently scanned under the fixed projection system to stitch together many projections over the full size of the wafer. We show results demonstrating control over the design space using small area test patterns with variations in the metasurface geometry. We also present the full-wafer large area demonstrator showing uniform performance within the design specifications.

A particular feature of the design is the use of transparent conducting oxide Al-doped ZnO (AZO), which forms a promising material class for tailoring the response in the mid-IR through its strong dispersion of optical properties from dielectric to metallic regime across the bulk plasmon frequency. These are large-bandgap semiconductors with free electrons in the range of  $10^{19}$ – $10^{21}$  cm<sup>-3</sup>.<sup>[62,63]</sup> Infrared metasurfaces based on conducting oxides have so far been reported to operate in the broadband range<sup>[18,64]</sup> and it is a challenge to form a multi-band infrared metasurface using AZO. We report here a design using a novel 5-layer stack incorporating a thin Ti layer and the AZO metasurface as characteristic features. We explore the potential for extending the design space using the particular sets of materials and design stack of this work, which is beneficial to achieve a wide range of parameters with a single underlying design principle and opens up a platform for tailoring infrared responses that can be achieved using a single process workflow and technology qualification.

## 2. Results and Discussion

### 2.1. Design and Numerical Results

The main attribute of the proposed meta-surface is that it controls the infrared emissivity or equivalently, reflectivity, of an incident electromagnetic wave in two different spectral bands corresponding to the response of typical infrared imaging

equipment covering the two atmospheric windows (3–5 μm labeled  $R_{MW}$ , and 8–13 μm labeled  $R_{LW}$  reflectivities). The proposed metasurface design process is based on the principles of operation of metallo-dielectric periodic structures but also exploits to a large extent the dispersion of material response with the wavelength in order to effectively control electro-optic (EO) emissivity with a broadband response within each of the two spectral windows of interest.

Achieving an arbitrary difference in the reflectance or emissivity response between the two spectral windows is a non-trivial task that is challenging to achieve using conventional materials and designs. Our design principle involves a multilayer Salisbury screen stack with a thin Ti-film, sensitively controlling the coupling between the top and bottom dielectric spacer. Strong dispersion properties of Ti between the MWIR and LWIR range provide a convenient spectrally selective mechanism. Strong material dispersion is also offered by the low-conductivity AZO material, which is intentionally tailored to achieve spectrally broad, resonant plasmonic features in the LWIR while having dielectric characteristics in the MWIR band.

The IR metasurface design is schematically shown in **Figure 1a,b**, showing a 3D view and corresponding cross-section of the stack. From bottom to top, the stack consists of an 80 nm aluminum (Al) back-reflector, a 1 μm thick silica (SiO<sub>2</sub>) spacer, the thin titanium (Ti) layer, a 350 nm thick alumina (Al<sub>2</sub>O<sub>3</sub>) layer and the 150 nm thick metasurface made of AZO periodically arranged square features. The critical layer in the overall design is the AZO metasurface. The metasurface fulfills two essential roles: first, the metasurface is used to create an artificial impedance that is controlled by changing the dimensions of the square features and their gap, and second, we take advantage of the partial absorption of radiation due to the low conductivity of the AZO.

The percentage of reflection of each spectral band determines the sequence in which the remainder of the layers are stacked (see Section S2, Supporting Information, for the loss contribution from each individual layer). Aiming to absorb the incident electromagnetic wave by more than 90% in the spectral band 8–13 μm ( $R_{LW} < 10\%$ ), we must match the upper layer's impedance to the impedance of free space (377 Ω). This matching allows the wave to propagate within the structure. The complex refractive index of SiO<sub>2</sub> presents an abrupt fluctuation at a wavelength of around 9.5 μm, which results in the partial absorption of the radiation and affects the impedance matching between the layers. Thus, another part of the radiation is reflected. To mitigate the dispersion of SiO<sub>2</sub>, we place it directly above the ground plane. Then, we place a very thin layer of Ti where in the 3–5 μm spectral band, the values of the complex refractive index  $n$  are about 4.5 and  $k$  assumes values ranging from 5.9–9.2 while in the spectral band 8–13 μm,  $n$  covers values from 5.8 to 9.1 and  $k$  gets values from 14.8 to 21.3. The Ti thickness, therefore, critically affects the EO response in the two bands (see Section S3, Supporting Information, for more details). Above the Ti-film, we place a second, thinner spacer for which Al<sub>2</sub>O<sub>3</sub> was selected as the material most compatible with the fabrication process. Other choices of dielectrics are discussed further below.

For the metasurface, we choose AZO with a carrier density of  $6 \times 10^{20}$  cm<sup>-3</sup>, consistent with our previous works and the

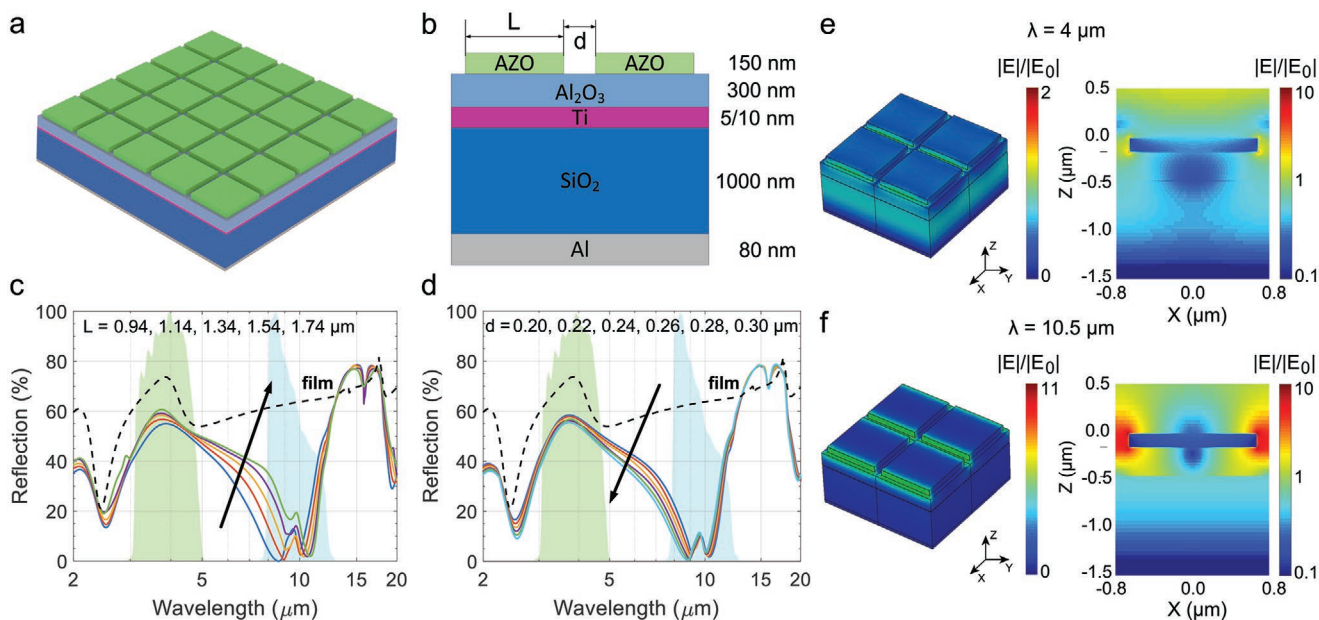


**Figure 1.** AZO metasurface with multi-band response. a) 3D schematic of the metasurface. b) Cross-section of the designed metasurface. c) Simulated spectra of the metasurfaces with various feature sizes  $L$  and a fixed  $d = 0.2 \mu\text{m}$ . d) Simulated spectra of metasurfaces with  $d$  from 0.20 to 0.30  $\mu\text{m}$  and a fixed feature size of 1.34  $\mu\text{m}$ . All simulations are for 5 nm Ti-film. Shaded areas represent the two detector bands used for experimental evaluation. e, f) Near-field maps at selected wavelengths of 4 and 10.5  $\mu\text{m}$  showing the electric field amplitude normalized to the input  $|E|/|E_0|$  both in the 3D isometric view of four unit cells (linear scale) and in the cross-sectional view (logarithmic scale) through the center of one of the metasurface elements.

highest carrier density achieved in our experimental system.<sup>[63]</sup> The metasurface (Figure 1b) is designed as a square array of AZO features with varying sizes and gap spacing between adjacent structures. Figure 1c shows the simulated optical response of the complete design for various feature sizes from 0.94 to 1.74  $\mu\text{m}$  and a fixed gap size of 0.2  $\mu\text{m}$ . Here, a Ti thickness of 5 nm was used. For the 1.34  $\mu\text{m}$  structure with a 0.2  $\mu\text{m}$  gap, a reflection of around 50% is achieved in the MWIR range (3–5  $\mu\text{m}$ ), whilst a lower reflection of  $\approx 10\%$  is achieved in the LWIR range (8–13  $\mu\text{m}$ ). The surface impedance in the MWIR range (3–5  $\mu\text{m}$ ) is around 1600  $\Omega$  while in the LWIR range (8–13  $\mu\text{m}$ ), where the reflection is around 10%, the impedance is around 390  $\Omega$ . If there is a mismatch between the impedance of free space and the surface impedance, the absorption/reflection depends on the upper layer of the structure. The wave penetrates to a greater depth when there is a match between the aforementioned impedances—the absorption peak in the LWIR range shifts along with the increase in feature size. We observe a similar effect on optical response in Figure 1d when tuning the gap from 0.20 to 0.30  $\mu\text{m}$ , with a fixed feature size of 1.34  $\mu\text{m}$ .

Further investigation of the dependence of the reflectivity on the thickness of both  $\text{SiO}_2$  and  $\text{Al}_2\text{O}_3$  dielectric layers is presented in Figure S3, Supporting Information. Both dielectrics are important in setting up maximum reflectivity in the MWIR range. The strong absorption feature in the LWIR band (i.e., low reflectivity in Figure 1c,d) can be attributed to the plasmonic resonance effects of the AZO metasurface. Figure 1e,f shows the electric near-field enhancements  $|E|/|E_0|$  around the nanostructured surface for selected wavelengths of 4 and 10.5  $\mu\text{m}$ , both in isometric 3D plots, as well as in cross-sectional maps through the center of the AZO feature (logarithmic scale).

The combined metal-insulator-metal (MIM) stack of the AZO metasurface/ $\text{Al}_2\text{O}_3$ /Ti structure forms a metamaterial-perfect absorber<sup>[8]</sup> configuration with a pronounced optical resonance in the LWIR. The near-field map at 10.5  $\mu\text{m}$  wavelength indeed shows one order local field enhancement around the structure characteristic for the dipolar (half-wavelength) resonance mode of the AZO feature. In comparison, at 4  $\mu\text{m}$  wavelength, the AZO metasurface does not show any significant resonance effects, furthermore, fields are seen to propagate through the semitransparent Ti-film into the underlying  $\text{SiO}_2$  layer.

## 2.2. Fabrication and Optical Characterization of Metasurfaces

Our experimental studies report results for two full-size 200 mm wafer demonstrators. In the first wafer fabrication run, various DUV doses from 14 to 28  $\text{mJ cm}^{-2}$  were tested to achieve the designed feature size. In the second wafer fabrication run, the optimized dose of 20  $\text{mJ cm}^{-2}$  has been applied uniformly to the entire wafer. The Ti thickness has been increased slightly from 5 to 10 nm for this run to protect against variability due to the lack of optimum control of thickness. Wafers were prepared as detailed in the Experimental Section.

The variable dose wafer is presented in Figure 2a, consisting of a large area of universal design ( $L = 1.34 \mu\text{m}$  and  $d = 0.2 \mu\text{m}$ ) over most of the wafer, except for a 16 mm wide stripe region over the middle of the wafer containing small test areas with a range of  $L$  and  $d$  variations. The dose was increased from the bottom right to the top left of the image. Figure 2b shows a typical top-view scanning electron microscopy (SEM) image of the AZO metasurface with a DUV exposure dose of 20  $\text{mJ cm}^{-2}$ . The features are well separated, showing that the exposure

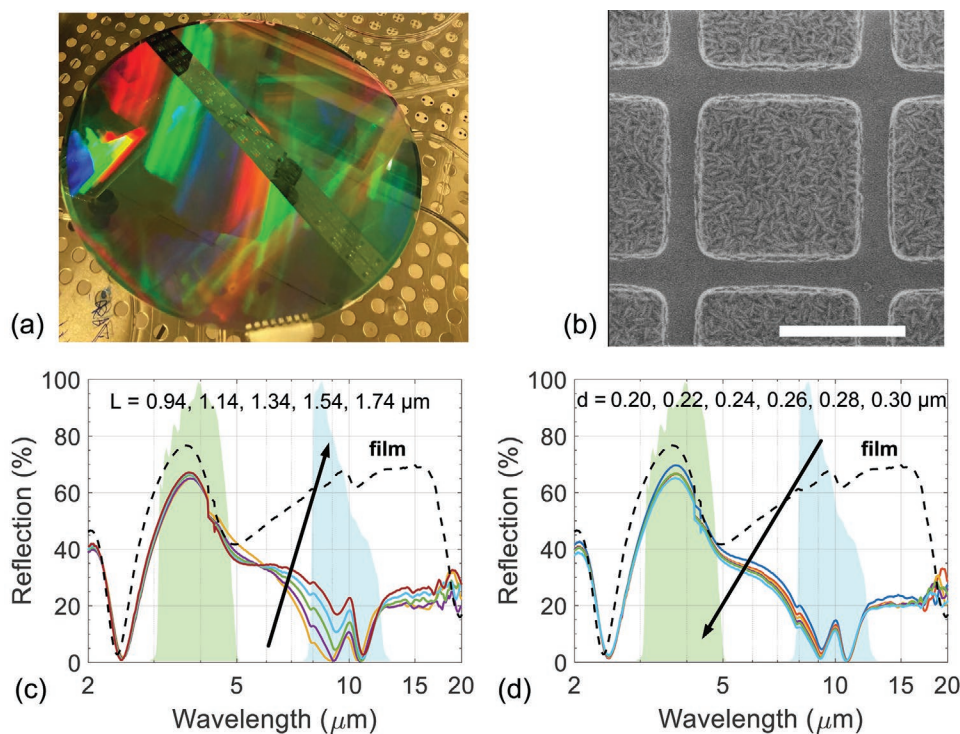


**Figure 2.** AZO metasurface fabricated using variable DUV exposure doses and 5 nm Ti. a) Photograph of the 200 mm (8-in.) metasurface; b) top-view SEM image of metasurface with nominal  $L = 1.34 \mu\text{m}$  and  $d = 0.2 \mu\text{m}$  defined by  $20 \text{ mJ cm}^{-2}$  DUV exposure dose. SEM scale bar is  $1 \mu\text{m}$ . c) Experimental FTIR spectra of metasurfaces with  $L$  from  $0.94$  to  $1.84 \mu\text{m}$  with a step of  $0.2 \mu\text{m}$ . d) Experimental FTIR spectra of metasurface with  $d$  from  $0.2$  to  $0.30 \mu\text{m}$  with a step of  $0.02 \mu\text{m}$  and fixed  $L = 1.34 \mu\text{m}$ . Shaded areas represent the two detector bands used for further evaluation.

dose is sufficient. Corresponding SEM images of arrays with different exposure doses, as well as characterization of the fabricated versus design dimensions are presented in Section S4, Supporting Information.

The dose of  $20 \text{ mJ cm}^{-2}$  was subsequently used for the whole wafer metasurface with homogeneous coverage. Figure 2c shows experimental spectra of metasurfaces with  $L$  from  $0.94$  to  $1.74 \mu\text{m}$  and  $d = 0.2 \mu\text{m}$ . The spectra of an unpatterned AZO film with an identical stack structure are also presented for comparison. All arrays show a consistent MWIR reflectivity of around  $60\%$  but varying reflectivity in the LWIR range. With the increase in size  $L$ , the peak around  $9 \mu\text{m}$  becomes narrower and lower and thus the smaller feature size is preferred for lower overall reflectivity in the LWIR range. Compared with the unpatterned AZO film, reflections of metasurfaces in the LWIR are significantly reduced owing to their resonantly enhanced absorptions around the resonance wavelength of the structured metasurface. In agreement with simulated results (Figure 1c), experimental spectra show a maximum reflectivity in the MWIR band centered around  $3.5 \mu\text{m}$  wavelength, which is attributed to the variation in skin depth of the 5 nm Titanium film.

The variation of response with the metasurface gap size is presented in Figure 2d for a fixed  $L = 1.34 \mu\text{m}$ . The dependence on gap size in this limited range is quite small but confirms that the smaller gap sizes are the most appropriate for achieving the favored response, that is, a high reflectivity in the MWIR and low reflectivity in LWIR. In all experimental curves, we note that the reflectivity at longer wavelengths from  $13\text{--}20 \mu\text{m}$

does not reach as high as in the simulations of Figure 1c,d for the patterned metasurfaces, while the thin-film stack only shows a strong reduction above  $18 \mu\text{m}$ . We attribute this difference to a metasurface-induced additional absorption in experiments, which is not fully captured by our model. As the region lies outside of the two bands of interest, we do not further consider this discrepancy in our analysis.

The dual-band reflectivities in MWIR and LWIR,  $R_{\text{MW}}$  and  $R_{\text{LW}}$ , are calculated by averaging the reflection over the respective spectral bands. For direct comparison with the results presented further below, the individual wavelengths are weighted against the response function of the reflectometer used in the directional hemispherical reflective measurements, as discussed in detail in the Experimental Section. This response function is very similar to the response function of commonly used infrared sensors and imagers used in real-world applications. Extracted values are  $R_{\text{MW}} = 55.7\% \pm 0.3\%$  independent of gap size  $d$  or feature size  $L$ . The long wave response is significantly influenced by the feature size though and  $R_{\text{LW}}$  decreases from  $18.1\%$  to  $5.6\%$  with decreasing feature size.

To demonstrate a wafer-scale large metasurface, a design of  $L = 1.34 \mu\text{m}$  and  $d = 0.2 \mu\text{m}$  and a fixed exposure dose of  $20 \text{ mJ cm}^{-2}$  was chosen to process a 200 mm substrate with a uniform metasurface covering its entire surface. Figure 3a shows a photograph of the fabricated wafer-scale large metasurface. The metasurface looks uniform with light scattering, with no clear contrast change except for a single exposure defect at the 4 o'clock direction on the image. Figure 3b shows a typical

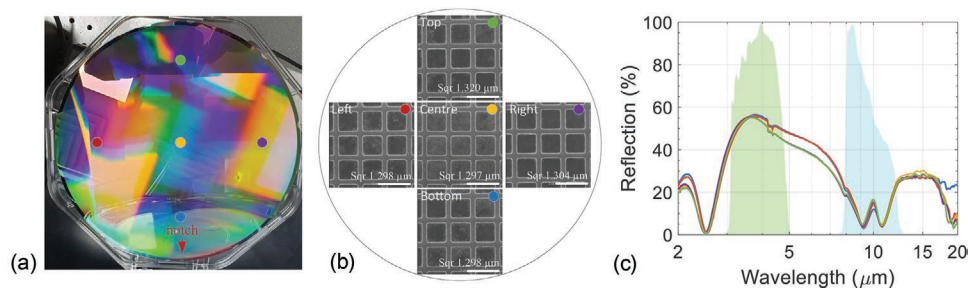


**Figure 3.** AZO metasurface fabricated using a fixed exposure dose and 10 nm Ti thickness. a) Photograph of a 200 mm (8-in.) metasurface fabricated with a fixed 20 mJ cm<sup>-2</sup> DUV exposure dose and 10 nm Ti; b) planar SEM images taken over different locations over the wafer. SEM bar is 2 μm. c) Experimental FTIR spectra of the metasurface at different locations on the wafer; shaded areas represent the two detector bands used for further evaluation.

SEM image of the fabricated metasurface. The feature sizes of the metasurfaces at different regions over the substrate have a very narrow distribution of  $L = 1.30 \pm 0.05 \mu\text{m}$ , which is attributed to the high uniformity process tools used, for example, the DUV scanner and ion beam etcher. The cross-section SEM image is provided in Section S5, Supporting Information. The reflection spectra at different regions are presented in Figure 3c. High consistency is seen in the 8–13 μm region, whilst some variation is noticeable in the range between 4 to 8 μm. Reflectivities  $R_{\text{MW}}$  and  $R_{\text{LW}}$  were again extracted. Variations are low with  $R_{\text{MW}}$  at  $51.3 \pm 0.9\%$  and  $R_{\text{LW}}$  at around  $11.0 \pm 0.4\%$ , indicating an excellent performance uniformity from a uniformly fabricated large-scale metasurface. Both values are slightly inferior to the maximum values achieved on the variable dose wafer, due to trade-offs in manufacturing risk against performance, specifically the slightly thicker Ti-film of 10 nm instead of 5 nm. We note that the slightly thicker film gives a flatter response over the bands, which could be a performance metric, as discussed in the Discussion section.

### 2.3. Directional Hemispherical Reflectance Analysis

To further characterize the response of the devices, a number of characterizations were done using accepted standardized methods. Directional hemispherical reflectance (DHR) measurements were taken for both wafers at 20° and 60° using a commercial multi-band reflectometer (SOC-410). Figure 4a shows the LWIR thermal image of the first metasurface wafer with variable exposure doses and for the 5 nm Ti-film. The exposure dose is increasing from the right side to the left side as columns in the presented orientation of the wafer. In the thermal image, the substrate is homogeneously bright in most areas except the four columns from the right in dark contrast. As presented in Section S4, Supporting Information, the right four columns are underexposed, and thus, the metasurface is not well-defined in those regions. Beyond the right four columns, column borders are barely seen, indicating an excellent overlapping control to almost eliminate stitching artifacts in the tile-like DUV exposure regions. DHR measurements were performed in seven positions marked by colored spots and numbered from 1–7, with DHR values presented in Figure 4b. The DHR values of positions 4–7 in the 3–5 μm band ( $R_{\text{MW}}$ ) consistently lie around 55% and 45% for angles of 20° and 60°, respectively, while DHR values of underexposed

positions 1–3 are only slightly higher. In the 8–13 μm band ( $R_{\text{LW}}$ ), DHR values of sufficiently exposed positions 4–7 are around 15% and 21% for angles of 20° and 60°, respectively, while underexposed positions give much higher values at both angles. This higher reflectance is attributed to the effect of the improperly formed metasurface, which resembles the response of the continuous thin film. The DHR values of 0° can be calculated from FTIR measurements with calculations detailed in the Experimental Section and Section S6, Supporting Information, under the assumption that scattering outside of the collection angle (numerical aperture 0.58) of our FTIR microscope is small. Figure 4c compares the FTIR and multi-band reflectometer measurements (red, blue symbols) and simulated values (lines see simulated spectra in Section S7, Supporting Information). The FTIR and reflectometer measurements show an excellent agreement with the simulated results.

Figure 4d shows the thermal image of the second wafer-scale metasurface, with a fixed exposure dose of 20 mJ cm<sup>-2</sup> and 10 nm Ti thickness, with corresponding DHR values shown in Figure 4e,f. A homogeneous brightness is seen over the whole substrate with no tile borders of the DUV wafer scanner exposure identified, which indicates that a highly uniform optical metasurface is achieved over the entire diameter of 200 mm. DHR measurements were performed at four different positions, which are marked by the colored dots in Figure 4d and presented in Figure 4e. The measured DHR values consistently lie around 46% and 42% for angles of 20° and 60°, respectively, in the 3–5 μm ( $R_{\text{MW}}$ ) band and 13% and 20% for angles of 20° and 60°, respectively, in the 8–13 μm ( $R_{\text{LW}}$ ) band. Figure 4f again compares DHR values measured from multi-band reflectometer, FTIR, and simulated values (with simulated spectra in Section S7, Supporting Information). These results are consistent with our FTIR measurements (Figure 3) which indicate  $R_{\text{MW}}$  around 50% and  $R_{\text{LW}}$  around 10% for this wafer-scale metasurface. Like those for the 5 nm Ti substrate, the  $R_{\text{MW}}$  and  $R_{\text{LW}}$  for the 10 nm Ti substrate are also in good agreement with simulations.

### 2.4. Exploration of Design Space: Random Designs

In the previous sections, we demonstrated a specific design aimed at achieving a low reflection or high emissivity in the thermal LWIR band combined with a high reflectivity contrast in the MWIR band. The 5-layer stack was conceived from

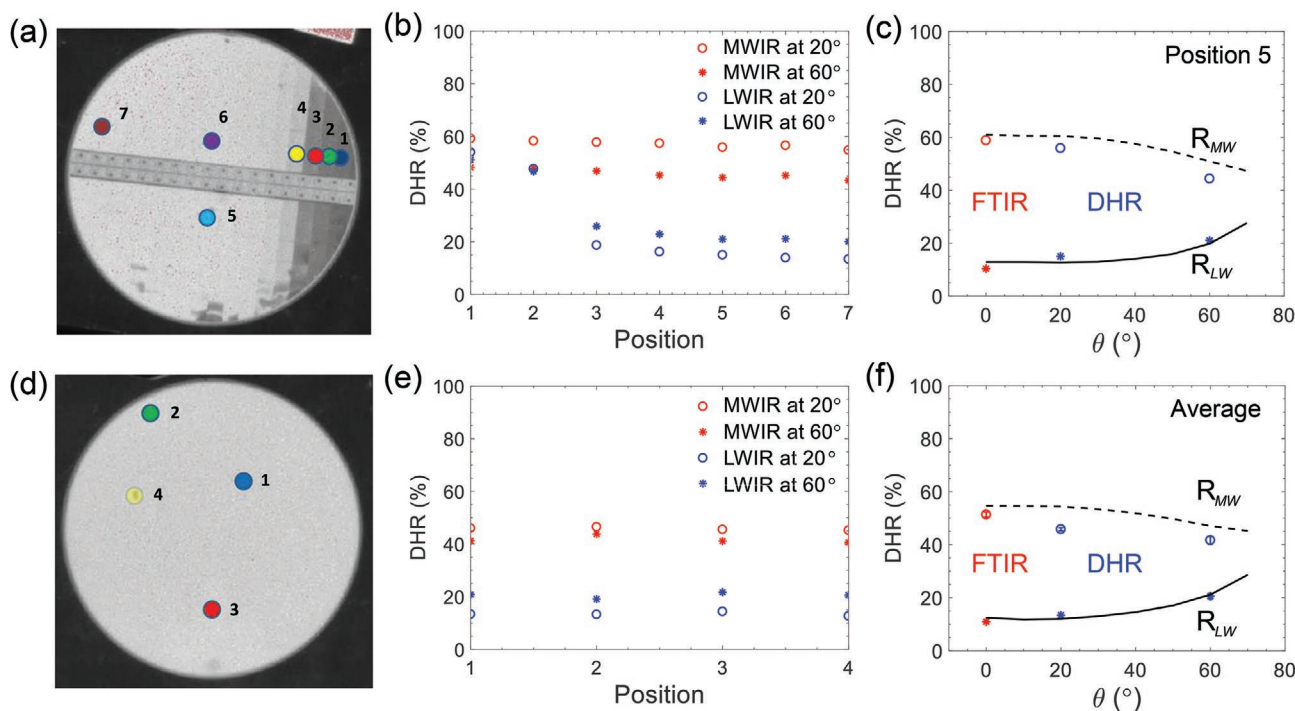


**Figure 4.** a) Thermal (LWIR) image of the metasurface with gradient exposure dose and 5 nm Ti. b) Experimental directional hemispherical reflectance (DHR) of the wafer in (a). c) Experimental (dots) and simulated (lines) MWIR and LWIR reflectivities of position 5 against different incident angles  $\theta$ . d) Experimental thermal image of the metasurface with a fixed exposure dose and 10 nm Ti, and e) experimental DHR of the wafer in (d). f) Experimental (dots) and simulated (lines) MWIR and LWIR reflectivities of the four positions in (d) against different incident angles  $\theta$ .

rational design principles inspired by concepts taken from the microwave domain. It is particularly useful to assess whether the same basic design allows to achieve a variation in the dual-band EO response by simply altering layer thicknesses and in-plane metasurface parameters. Such a flexible platform for designing EO responses using a set of common materials and fabrication methods would hold significant advantages with respect to manufacturability and technology qualification for specific application domains such as space or defense.

The design space for the 5-layer metasurface stack has six freely tunable parameters (four layer thicknesses and two metasurface geometric parameters). To explore this space, we first evaluated 3000 random designs with parameters set by the physical constraints in layer thickness and patterning capabilities of the tools used in this work. We evaluated thicknesses of the bottom and top dielectric of 500–1500 nm and 200–1000 nm respectively, a Ti-film thickness ranging from 4–150 nm, and AZO thickness from 0–400 nm. For the in-plane metasurface, we chose square features with individual sizes of 300–1300 nm and gaps ranging from 200–500 nm. Results are given by the red open circles in **Figure 5a**, which show the joint distribution of mid-wave and long-wave IR reflectivity values  $R_{MW}$  and  $R_{LW}$ . The basic 5-layer perfect metamaterial absorber (PMA) design allows for structures covering a considerable range of the parameter space within the physically realistic parameter range. We furthermore note that the experimental demonstrator metasurface (PMA) device with  $R_{MW} = 60\%$ ,  $R_{LW} < 10\%$  corresponds to the bottom right corner of the parameter space, as also shown in panel (i) of **Figure 5c**, indicating that this is indeed a

nontrivial example that pushes the boundaries of the conceptual design.

The benefit of metasurface patterning is illustrated by comparing it with a set of equivalent unpatterned thin-film stacks without metasurface patterning. The results for unpatterned devices are given by the green open circles in **Figure 5a** and show a very limited coverage of the design space limited to the top right of the range with both high  $R_{MW}$  and  $R_{LW}$ , which is attributed to the much-reduced tunability of the surface impedance in this case. The high LWIR reflectivity of the thin-film design was already seen experimentally in **Figure 2**. Obtaining high reflectivities in both spectral bands may indeed be considered a trivial challenge that can be fulfilled with many conventional thin-film or metallic reflector designs.

Next, to demonstrate the benefit of the Ti reflection layer, we compare it with a set of calculations without Ti-film, as indicated by the yellow open circles in **Figure 5a**. Without the Ti-film, the design space is essentially reduced to that of a conventional Salisbury screen with a single dielectric spacer consisting partially of  $\text{SiO}_2$  and  $\text{Al}_2\text{O}_3$ . For this type of design, higher values of  $R_{MW}$  are achieved; however, at the cost of a reduced parameter space coverage.

A performance figure of importance in some applications is the flatness of the response over the spectral window, as often a uniform response within the selected band is desired. In **Figure 5b**, we plot the standard deviation of the reflectance ( $\sigma_{MW}$ ,  $\sigma_{LW}$ ) for the same datasets. The standard deviation is defined from the absolute reflectivity in the bands, that is, without any spectral weighting. The solutions cover a range of

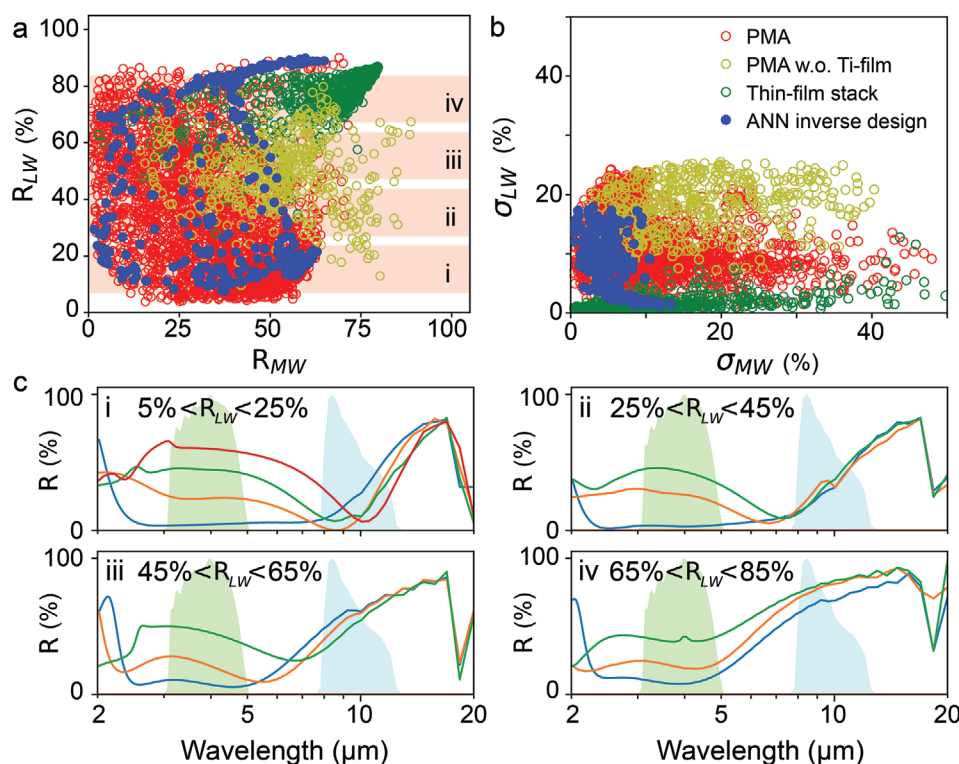


**Figure 5.** a) Simulated distribution of reflectance values ( $R_{MW}$ ,  $R_{LW}$ ) in two spectral bands corresponding to 3–5  $\mu\text{m}$  and 8–13  $\mu\text{m}$ , weighted with IR detector response functions (shaded areas). Red open circles: randomly generated metasurface stack designs over six design degrees of freedom. Yellow open circles: random designs without Ti-film. Green open circles: unpatterned thin-film designs with Ti film. Blue dots: ANN inverse design results. b) Corresponding flatness of response characterized by standard deviations ( $\sigma_{MW}$ ,  $\sigma_{LW}$ ) for the same simulated dataset. c) Examples of ANN-generated spectra with flat spectral response (minimized  $\sigma_{MW}$ ,  $\sigma_{LW}$ ), sorted into four bands (i–iv) of  $R_{LW}$  levels with 0.2 bin width. Shaded areas correspond to IR detector response curves for mid-wave (green) and long-wave (blue).

standard deviations from 0 up to 50%, where the higher values indicate poor flatness. Typically, flatness values below 10% would correspond to a reasonably smooth spectral response within each band. Generally, the distribution of flatness in the 8–13  $\mu\text{m}$  (LWIR) is better than in the 3–5  $\mu\text{m}$  (MWIR) range, and the devices without Ti-film show a less flat behavior than those with Ti-film. The thin-film stacks are very flat in the LWIR response because they act as a simple mirror in this range.

## 2.5. Deep Learning Neural Network Inverse Design

To achieve a more controlled inverse design of the dual-band reflectors, we made use of an artificial neural network (ANN) approach. We follow here the general approach presented in our previous work<sup>[65]</sup> using a tandem encoder-decoder scheme based on the ResNet ANN to test the inverse design of a range of devices covering the ( $R_{MW}$ ,  $R_{LW}$ ) space. As the tandem ANN is trained on the inverse problem, it directly outputs a design structure for any combination of target objectives. Flat spectral bands with minimized standard deviations ( $\sigma_{MW}$ ,  $\sigma_{LW}$ ) are achieved by using the full spectrum within the two bands as input for the target response. Details of the model are presented in Section S8, Supporting Information.

Results for the ANN generated designs are shown in Figure 5a,b as the solid blue dots. These solutions were

generated using 20 equally spaced target values each for  $R_{LW}$  and  $R_{MW}$  (i.e. 2% steps in both) as input parameters, thus resulting in a grid of 400 target combinations. It is seen that the inferred designs do not project onto this grid, but rather the solutions trace out a particular pattern in parameter space, which is characterized by a band of closely lying solutions with larger gaps in between. The characteristic contour of inferred solutions is a combination of two main features, namely i) that physical solutions with good spectral flatness can be found primarily on this contour, and ii) the tandem ANN has a tendency to collapse onto a single set of solutions in parameter space. The latter is a well-known feature of this type of ANN, which has been critically discussed elsewhere.<sup>[66]</sup>

Importantly, the solutions inferred by the ANN inverse design show a significantly improved flatness as compared to the randomly generated dataset, as shown in Figure 5b. Figure 5c shows selected spectra from the solutions inferred by the ANN over four different ranges of values for  $R_{LW}$ , as shown in panels (i–iv), and up to four for  $R_{MW}$ , as indicated by the different colored spectra in each panel, where each spectrum represents a design with the flattest spectral response within this range. Overall, the solutions appear smooth over the two ranges of interest, where we point out that the bending of the spectral response above 12  $\mu\text{m}$  is a consequence of the dispersion of the  $\text{Al}_2\text{O}_3$ . Solutions with larger bandwidth in the LWIR spectral range can be obtained by substituting a material with



lower dispersion in this range, such as Ge, as discussed in Section S10, Supporting Information.

## 2.6. Comparison with State-of-the-Art

Our experimental and computational study has focused on achieving a platform for tailoring the infrared response in the two atmospheric bands at 3–5  $\mu\text{m}$  and 8–13  $\mu\text{m}$ . As briefly discussed in the Introduction, other works have investigated metasurface-based approaches targeting specific functionalities. A more general overview of single-frequency and broad-band metasurface perfect absorbers has been the subject of several high-quality reviews.<sup>[8,21]</sup> **Table 1** shows the state-of-the-art literature on dual-band infrared functional coatings, exploiting metasurface design degrees of freedom. Many of these focus on the use of narrowband antenna structures made from metals Al, Ag, and Au, where either multiple antennas are combined or a single antenna is shaped to provide multiple resonances. Notable is also the use of complementary structures, such as hole arrays, to achieve a frequency selective surface with resonance absorption in the visible and near-infrared combined with high reflectivity over a large spectral band.<sup>[51]</sup> In order to achieve additional radio-frequency (RF) or microwave functionalities, multi-scale patterning is employed, where micrometer-scale and millimeter-scale structural features are sufficiently far apart in size to allow their separate definition without cross-talk.<sup>[50]</sup>

Our generalized approach is distinct from specific applications that focus on achieving high reflectivity in the two atmospheric windows combined with one or more resonant absorption features and/or RF functionality,<sup>[15,46,50,51]</sup> as well

as from those aiming to synthesize multiple high optical absorption/emissivity through embedding multiple resonators<sup>[32,34,42,53]</sup> or multi-resonance antennas.<sup>[31,37,41,54]</sup> Our approach specifically addresses the problem of achieving arbitrary average reflectivities with a flat spectral response, which is not easily obtained using multi-resonance synthesis.

The overview in Table 1 also includes the minimum dimension size and device area that is explicitly demonstrated in the respective works. A wide variety in feature sizes from 100 nm to several micrometers requires techniques ranging from EBL to photolithography, the latter of which can be more readily implemented at large surface areas. Our experimental demonstration involves minimum feature sizes of 200 nm and DUV scanner lithography, which fills a critical gap in fabrication capabilities between EBL and photolithography.

## 3. Conclusion

In conclusion, we have demonstrated a 200 mm wafer-scale infrared metasurface platform for the infrared using a CMOS-compatible fabrication method involving DUV lithography. By forming a 5-layer stack with the AZO metasurface on top, the device realizes distinctive optical responses in the 3–5  $\mu\text{m}$  MWIR and 8–13  $\mu\text{m}$  LWIR atmospheric windows, with a flat optical response within the bands. A homogeneous wafer-scale metasurface has been demonstrated with a reflectance of around 50% in MWIR and 10% in LWIR. Numerical simulations and deep learning inverse design show that the general design principle of the device allows for a wide range of reflectivity within the atmospheric windows to be realized using a common platform of materials and fabrication workflow. There

**Table 1.** Overview of the state-of-the-art in infrared dual-band functional coatings.

Type of response	Sim/Exp	Design approach	Narrow/broadband	Materials	Fabrication, feature size	Device area	Ref.
Tunable narrow abs. 3–20 $\mu\text{m}$	Exp	Multi-res. antenna	Narrow	Au, MgF <sub>2</sub>	EBL, 100 nm	<1 mm <sup>2</sup>	[41]
3–5 $\mu\text{m}$ , 8–12 $\mu\text{m}$ , high abs.	Exp	Multiple antennas		Au, Al <sub>2</sub> O <sub>3</sub>	EBL, 400 nm	4 × 4 mm <sup>2</sup>	[32]
	Sim	Multiple antennas		Au, Al <sub>2</sub> O <sub>3</sub>	N.A.	N.A.	[53]
	Exp	Accordion antenna		Au, MgF <sub>2</sub>	NIL, 100 nm	8 × 8 mm <sup>2</sup>	[37]
Multi-resonance 8–12 $\mu\text{m}$ , high abs.	Exp	MIM	Multi-resonance synthesis	Al, Al <sub>2</sub> O <sub>3</sub> , ZnSe	Photolith., 3.19 $\mu\text{m}$	Not specified	[54]
Multi-resonance 3–5 $\mu\text{m}$ , high abs.	Exp	Multiple antennas		Au, Al <sub>2</sub> O <sub>3</sub>	EBL, 850 nm	10 × 10 mm <sup>2</sup>	[34,42]
Multi-resonance 3–5 $\mu\text{m}$ , high abs.	Exp	Multi-res. antenna		Au, Kapton	EBL, 105 nm	Not specified	[31]
3–5 $\mu\text{m}$ and 8–14 $\mu\text{m}$ , high refl., 1.5 $\mu\text{m}$ , and 6–8 $\mu\text{m}$ high abs.	Sim	Coaxial resonator, MIM	Narrow	Ag, poly-imide	N. A.	N. A.	[15]
3–5 $\mu\text{m}$ and 8–14 $\mu\text{m}$ , high refl., 6.2 $\mu\text{m}$ , and 10.6 $\mu\text{m}$ , high abs.	Exp	Thin-film reflector and LWIR antenna		Si, GeSbTe, Au	Photolith., 5 $\mu\text{m}$	Not specified	[46]
3–15 $\mu\text{m}$ , high refl. and RF high abs.	Exp	Multi-scale patterning, hole array	Frequency selective surface	Au	Photolith., 1.65 $\mu\text{m}$	150 mm (6-in.)	[51]
8–12 $\mu\text{m}$ , refl., 5–8 $\mu\text{m}$ high abs., and RF high abs.	Exp	Multi-scale patterning, MIM	Narrow, hierarchic structuring	Au, ZnS	Photolith., 1 $\mu\text{m}$	100 mm (4-in.)	[50]
3–5 $\mu\text{m}$ and 8–13 $\mu\text{m}$ , tunable refl.	Exp	Metasurface, MIM stack, and material dispersion	Broadband impedance control	Al:ZnO, Al <sub>2</sub> O <sub>3</sub> , Ti, SiO <sub>2</sub>	DUV lith., 200 nm	200 mm (8-in.)	This work

Sim, simulation; Exp, experimental; EBL, e-beam lithography; NIL, nano-imprint lithography.

is a significant emerging research trend for utilizing atmospheric windows in new ways requiring different combinations of reflectivity and emissivity functionalities. We show here that metasurfaces can reach areas of this parameter space that are inaccessible through conventional materials. This study demonstrates a more generalized design and fabrication capability that is needed to adapt it to any application in the MWIR and LWIR atmospheric transparent windows. A general platform for achieving a wide range of reflectivity values in the infrared offers significant advantages in manufacturability, performance testing, and device qualification for a range of applications.

## 4. Experimental Section

**Fabrication of Metal Oxide IR Metasurfaces:** Metal oxide IR metasurface was fabricated onto 8-in. (200 mm) silicon substrates. The structure consisted of a sputtered aluminum film of 80 nm thickness as an optical back-reflector and then a 1000 nm SiO<sub>2</sub> spacer using the Bühler Helios sputtering system, followed by a thin titanium film of 5 or 10 nm using the Angstrom EVOVAC sputtering system. A 300 nm Al<sub>2</sub>O<sub>3</sub> was deposited and followed by 150 nm Al:ZnO using Oxford Instruments FlexAl ALD system. The Al<sub>2</sub>O<sub>3</sub> was grown at 175 °C using trimethylaluminum (TMA) and water. The Al:ZnO was grown at 250 °C using TMA and diethyl zinc (DEZ) and water with a TMA:DEZ cycle ratio of 4% (detailed in previous works)<sup>[18,63]</sup> and carrier concentration was measured to be  $6 \times 10^{20} \text{ cm}^{-3}$ . The AZO was subsequently patterned using Nikon NSR-S204B 248 nm DUV system with KrF M91Y photoresist (680 nm thickness after development). For the 5 nm Ti wafer, various exposure doses were varied from 14 to 24 mJ cm<sup>-2</sup> with a step of 2 mJ cm<sup>-2</sup>. For the 10 nm Ti wafer, the exposure dose of 20 mJ cm<sup>-2</sup> was used over the whole substrate. The AZO was subsequently etched using Oxford Instrument IonFab 300 plus ion beam etch (IBE) system with a pure Ar physical etch.<sup>[67]</sup> The etching rates were measured to be 6 nm min<sup>-1</sup> for AZO due to the micro-loading effect (small opening). The resist was subsequently stripped by an ultrasonic bath in NMP at 60 °C for about 11 h to ensure the removal of AZO redeposition during the IBE etch. The resist features and AZO features were planarly checked using Hitachi S8840 critical dimension SEM with cross-section checked by JEOL JSM-7500F.

**Optical Instrumentation:** The IR reflectance was measured in the range of 2 to 20 μm using an FTIR setup consisting of a Thermo-Nicolet Nexus 670 with a Continuum microscope, far-IR light source, KBr beam splitter, and nitrogen-cooled DTGS detector with a spot size of 100 × 100 μm<sup>2</sup>. For all measurements, an 80 nm aluminum-coated SiO<sub>2</sub>/Si substrate was used as a reference mirror.

In diffuse hemispherical reflectance experiments, the spectrally averaged total reflectivity  $R$  was measured, which was weighted with the SOC-410 DHR reflectometer response for each detection band. For consistency, all the reported  $R_{\text{MW}}$  and  $R_{\text{LW}}$  were chosen to weigh with these response functions, in order to allow direct comparison between simulations and experiments. The reflectivities of the two spectral bands were defined by  $R_{\text{MW}}$  and  $R_{\text{LW}}$  for the 3–5 and 8–13 μm ranges, respectively, using:

$$R_{\text{MW}} = \int_{3\mu\text{m}}^{5\mu\text{m}} R(\lambda)A(\lambda)d\lambda \quad (1)$$

$$R_{\text{LW}} = \int_{8\mu\text{m}}^{13\mu\text{m}} R(\lambda)A(\lambda)d\lambda \quad (2)$$

where  $R(\lambda)$  is the normalized reflectance,  $A(\lambda)$  is the absorption response of SOC-410 DHR reflectometer,<sup>[68]</sup> and  $\lambda$  is the wavelength.

DHR was measured at Malvern Optical Ltd. DHR was taken using a SOC-410 instrument. The SOC-410 collected data in six wavebands across the IR with a primary focus on 3–5 and 8–13 μm (corresponding

to MWIR and LWIR, respectively). DHR data were collected at two polar angles of 20° and 60° relative to the surface normal.

**Numerical Simulation:** For numerical simulations of metal oxide IR metasurface in the initial design, CST Microwave Studio was used, based on the finite integration technique. Although CST includes various electromagnetic solvers, the finite-element frequency-domain (FD) solver was chosen, as it could accurately calculate the electromagnetic response of a periodic structure for an ultra-broad spectral band. Furthermore, it was the only solver that an oblique angle of incidence could be considered. An additional feature of the FD solver includes periodic boundary conditions that can be applied to arbitrarily shaped unit cells, assuming infinite size structures and introducing the phase shift between elements.

**Parameter Studies and Neural Network Design:** For numerical simulations in the parameter studies, Ansys Lumerical FDTD Solutions was used. A wide range of spectra were generated for different device parameters. The deep learning neural network was a tandem network consisting of a pre-trained forward network and an inverse network. Each of the networks was implemented using an encoder-decoder layout. Details of the network architecture and hyperparameters are given in Section S8, Supporting Information.

## Supporting Information

Supporting Information is available from the Wiley Online Library or from the author.

## Acknowledgements

The authors acknowledge the funding from DASA/Dstl under Grant Award No. ACC6011239. O.L.M. acknowledges the support from EPSRC grant EP/M009122/1. The authors acknowledge Malvern Optical Ltd for its support with Directional hemispherical reflectance (DHR) measurements and useful discussions with Dr. Peter Raven from Malvern Optical Ltd. The authors thank the Southampton “Cornerstone” wafer-scale processing facility for its expertise in DUV lithography.

## Conflict of Interest

The authors declare no conflict of interest.

## Data Availability Statement

All data supporting this study are openly available from the University of Southampton repository at DOI: <https://doi.org/10.5258/SOTON/D2141>.

## Keywords

electro-optical devices, emittance control, infrared materials, metasurfaces, plasmonics

Received: February 25, 2022

Revised: April 26, 2022

Published online: June 19, 2022

[1] M. Papaioannou, E. Plum, J. Valente, E. T. F. Rogers, N. I. Zheludev, *Light: Sci. Appl.* **2016**, *5*, e16070.

[2] T. Cui, B. Bai, H.-B. Sun, *Adv. Funct. Mater.* **2019**, *29*, 1806692.

- [3] Y. Yang, I. I. Kravchenko, D. P. Briggs, J. Valentine, *Nat. Commun.* **2014**, *5*, 5753.
- [4] M. K. Chen, Y. Wu, L. Feng, Q. Fan, M. Lu, T. Xu, D. P. Tsai, *Adv. Opt. Mater.* **2021**, *9*, 2001414.
- [5] N. Yu, F. Capasso, *Nat. Mater.* **2014**, *13*, 139.
- [6] A. Arbabi, Y. Horie, M. Bagheri, A. Faraon, *Nat. Nanotechnol.* **2015**, *10*, 937.
- [7] N. Yu, F. Aieta, P. Genevet, M. A. Kats, Z. Gaburro, F. Capasso, *Nano Lett.* **2012**, *12*, 6328.
- [8] C. M. Watts, X. Liu, W. J. Padilla, *Adv. Mater.* **2012**, *24*, OP98.
- [9] Y. Ra'di, C. R. Simovski, S. A. Tretyakov, *Phys. Rev. Appl.* **2015**, *3*, 037001.
- [10] C. L. Holloway, E. F. Kuester, J. A. Gordon, J. O. Hara, J. Booth, D. R. Smith, *IEEE Antennas Propag. Mag.* **2012**, *54*, 10.
- [11] X. Luo, *Sci. China Phys. Mech.* **2015**, *58*, 594201.
- [12] P. Su, Y. Zhao, S. Jia, W. Shi, H. Wang, *Sci. Rep.* **2016**, *6*, 20387.
- [13] S. W. Simms, V. F. Fusco, *2006 European Microwave Conf.*, September **2006**, <https://doi.org/10.1109/EUMC.2006.281165>.
- [14] H. Sun, C. Gu, X. Chen, Z. Li, L. Liu, B. Xu, Z. Zhou, *Sci. Rep.* **2017**, *7*, 40782.
- [15] J. Kim, K. Han, J. W. Hahn, *Sci. Rep.* **2017**, *7*, 6740.
- [16] B. M. Adomanis, C. M. Watts, M. Koirala, X. Liu, T. Tyler, K. G. West, T. Starr, J. N. Bringuier, A. F. Starr, N. M. Jokerst, W. J. Padilla, *Appl. Phys. Lett.* **2015**, *107*, 021107.
- [17] H. Cheng, S. Chen, H. Yang, J. Li, X. An, C. Gu, J. Tian, *J. Opt.* **2012**, *14*, 085102.
- [18] K. Sun, C. A. Riedel, Y. Wang, A. Urbani, M. Simeoni, S. Mengali, M. Zalkovskij, B. Bilenberg, C. H. de Groot, O. L. Muskens, *ACS Photonics* **2018**, *5*, 495.
- [19] A. D. Rakić, A. B. Djurišić, J. M. Elazar, M. L. Majewski, *Appl. Opt.* **1998**, *37*, 5271.
- [20] I. D. Mash, G. P. Motulevich, *Sov. Phys. JETP* **1973**, *36*, 516.
- [21] P. Yu, L. V. Besteiro, Y. Huang, J. Wu, L. Fu, H. H. Tan, C. Jagadish, G. P. Wiederrecht, A. O. Govorov, Z. Wang, *Adv. Opt. Mater.* **2019**, *7*, 1800995.
- [22] W. J. Padilla, *Spie Newsroom*, 14 October **2010**, <https://spie.org/news/3137-perfect-electromagnetic-absorbers-from-microwave-to-optical>.
- [23] X. Yin, R. Yang, G. Tan, S. Fan, *Science* **2020**, *370*, 786.
- [24] C. Zou, G. Ren, M. M. Hossain, S. Nirantar, W. Withayachumnankul, T. Ahmed, M. Bhaskaran, S. Sriram, M. Gu, C. Fumeaux, *Adv. Opt. Mater.* **2017**, *5*, 1700460.
- [25] S. Fan, W. Li, *Nat. Photonics* **2022**, *16*, 182.
- [26] Y. Nishijima, A. Balčytis, S. Naganuma, G. Seniutinas, S. Juodkazis, *Sci. Rep.* **2019**, *9*, 8284.
- [27] A. K. Osgouei, A. Ghobadi, B. Khalichi, E. Ozbay, *J. Opt.* **2021**, *23*, 085001.
- [28] J. Li, R. Gan, Q. Guo, H. Liu, J. Xu, F. Yi, *Opt. Express* **2018**, *26*, 16769.
- [29] J. Li, J. Li, S. Zhou, F. Yi, *Micromachines* **2021**, *12*, 1584.
- [30] Y. Gong, K. Li, N. Copner, H. Liu, M. Zhao, B. Zhang, A. Pusch, D. L. Huffaker, S. S. Oh, *Nanophotonics* **2021**, *10*, 1285.
- [31] Z. H. Jiang, S. Yun, F. Toor, D. H. Werner, T. S. Mayer, *ACS Nano* **2011**, *5*, 4641.
- [32] X. Liu, T. Tyler, T. Starr, A. F. Starr, N. M. Jokerst, W. J. Padilla, *Phys. Rev. Lett.* **2011**, *107*, 045901.
- [33] S. Jiang, J. Li, J. Li, G. Zhang, H. Liu, F. Yi, *Opt. Express* **2020**, *28*, 22617.
- [34] M. Makhsiyani, P. Bouchon, J. Jaeck, J.-L. Pelouard, R. Haïdar, *Appl. Phys. Lett.* **2015**, *107*, 251103.
- [35] G. Cao, H.-X. Xu, L.-M. Zhou, Y. Deng, Y. Zeng, S. Dong, Q. Zhang, Y. Li, H. Yang, Q. Song, X. Liu, Y. Li, C.-W. Qiu, *Mater. Today* **2021**, *50*, 499.
- [36] C. Wu, N. Arju, G. Kelp, J. A. Fan, J. Dominguez, E. Gonzales, E. Tutuc, I. Brener, G. Shvets, *Nat. Commun.* **2014**, *5*, 3892.
- [37] V. Nagal, T. Li, J. B. Khurgin, D. H. Gracias, *ACS Appl. Nano Mater.* **2020**, *3*, 7029.
- [38] A. Ahmadivand, B. Gerislioglu, *Laser Photonics Rev.* **2022**, *16*, 2100328.
- [39] D. Rodrigo, O. Limaj, D. Janner, D. Etezadi, F. J. G. d. Abajo, V. Pruneri, H. Altug, *Science* **2015**, *349*, 165.
- [40] A. Tittl, A. Leitis, M. Liu, F. Yesilkoy, D.-Y. Choi, D. N. Neshev, Y. S. Kivshar, H. Altug, *Science* **2018**, *360*, 1105.
- [41] K. Chen, R. Adato, H. Altug, *ACS Nano* **2012**, *6*, 7998.
- [42] H. T. Miyazaki, T. Kasaya, M. Iwanaga, B. Choi, Y. Sugimoto, K. Sakoda, *Appl. Phys. Lett.* **2014**, *105*, 121107.
- [43] L. Peng, D. Liu, H. Cheng, S. Zhou, M. Zu, *Adv. Opt. Mater.* **2018**, *6*, 1801006.
- [44] L. Xiao, H. Ma, J. Liu, W. Zhao, Y. Jia, Q. Zhao, K. Liu, Y. Wu, Y. Wei, S. Fan, K. Jiang, *Nano Lett.* **2015**, *15*, 8365.
- [45] K. Tang, X. Wang, K. Dong, Y. Li, J. Li, B. Sun, X. Zhang, C. Dames, C. Qiu, J. Yao, J. Wu, *Adv. Mater.* **2020**, *32*, 1907071.
- [46] M. Pan, Y. Huang, Q. Li, H. Luo, H. Zhu, S. Kaur, M. Qiu, *Nano Energy* **2020**, *69*, 104449.
- [47] Q. L. Kang, D. K. Li, W. Wang, K. Guo, Z. Y. Guo, *J Phys D Appl Phys* **2022**, *55*, 6.
- [48] H. Zhu, Q. Li, C. Tao, Y. Hong, Z. Xu, W. Shen, S. Kaur, P. Ghosh, M. Qiu, *Nat. Commun.* **2021**, *12*, 1805.
- [49] Z. Qin, C. Zhang, Z. Liang, D. Meng, X. Shi, F. Yang, *Adv. Photonics Res.* **2022**, *3*, 2100215.
- [50] T. Kim, J.-Y. Bae, N. Lee, H. H. Cho, *Adv. Funct. Mater.* **2019**, *29*, 1807319.
- [51] H. B. Shim, K. Han, J. Song, J. W. Hahn, *Adv. Opt. Mater.* **2022**, *10*, 2102107.
- [52] J. Kim, C. Park, J. W. Hahn, *Adv. Opt. Mater.* **2022**, *10*, 2101930.
- [53] E. Hou, Z. Qin, Z. Liang, D. Meng, X. Shi, F. Yang, W. Liu, H. Liu, H. Xu, D. R. Smith, Y. Liu, *Opt. Express* **2021**, *29*, 36145.
- [54] N. Zhang, P. Zhou, D. Cheng, X. Weng, J. Xie, L. Deng, *Opt. Lett.* **2013**, *38*, 1125.
- [55] Y. Wang, K. S. Kiang, M. Abb, O. L. Muskens, C. H. de Groot, *Microelectron. Eng.* **2015**, *141*, 87.
- [56] N. Meinzer, W. L. Barnes, I. R. Hooper, *Nat. Photonics* **2014**, *8*, 889.
- [57] M. Abb, Y. Wang, N. Papisimakis, C. H. de Groot, O. L. Muskens, *Nano Lett.* **2014**, *14*, 346.
- [58] A. Leitis, M. L. Tseng, A. John-Herpin, Y. S. Kivshar, H. Altug, *Adv. Mater.* **2021**, *33*, 2102232.
- [59] J.-S. Park, S. Zhang, A. She, W. T. Chen, P. Lin, K. M. A. Yousef, J.-X. Cheng, F. Capasso, *Nano Lett.* **2019**, *19*, 8673.
- [60] A. She, S. Zhang, S. Shian, D. R. Clarke, F. Capasso, *Opt. Express* **2018**, *26*, 1573.
- [61] T. Hu, Q. Zhong, N. Li, Y. Dong, Z. Xu, Y. H. Fu, D. Li, V. Bliznetsov, Y. Zhou, K. H. Lai, Q. Lin, S. Zhu, N. Singh, *Nanophotonics* **2020**, *9*, 823.
- [62] A. K. Pradhan, R. M. Mundle, K. Santiago, J. R. Skuza, B. Xiao, K. D. Song, M. Bahoura, R. Cheaito, P. E. Hopkins, *Sci. Rep.* **2014**, *4*, 6415.
- [63] K. Sun, W. Xiao, S. Ye, N. Kalfagiannis, K. S. Kiang, C. H. de Groot, O. L. Muskens, *Adv. Mater.* **2020**, *32*, 2001534.
- [64] S. Shrestha, Y. Wang, A. Overvig, M. Lu, A. Stein, L. Dal Negro, N. Yu, *ACS Photonics* **2018**, *5*, 3526.
- [65] N. J. Dinsdale, P. R. Wiecha, M. Delaney, J. Reynolds, M. Ebert, I. Zeimpekis, D. J. Thomson, G. T. Reed, P. Lalanne, K. Vynck, O. L. Muskens, *ACS Photonics* **2021**, *8*, 283.
- [66] P. R. Wiecha, A. Arbouet, C. Girard, O. L. Muskens, *Photon. Res.* **2021**, *9*, B182.
- [67] K. Sun, I. Zeimpekis, C. Hu, N. M. J. Ditshego, O. Thomas, M. R. de Planque, H. M. H. Chong, H. Morgan, P. Ashburn, *Microelectron. Eng.* **2016**, *153*, 96.
- [68] SOC 410 DHR Reflectometer User's Guide, Version CEA.2.1.2.4, Surface Optics Corporation, San Diego, CA **2019**.